

DINO: Dynamical Inspection of Newtonian Orbits

Modelling a basic disk-type galaxy

E. Canul*, A. A. Aroche **, G. Urrutia-Sánchez *** and G. Martínez-Bautista****

Instituto de Astronomía, Universidad Nacional Autónoma de México, AP 70-264, 04510 México DF, México

Received April 04, 2016; accepted June 10, 2016

ABSTRACT

Context. With current surveys we can obtain a huge amount of data about galactic nature. One of the most interesting subject is the dynamical galactic evolution, where the mass, rotation velocity, and stellar populations play an important role. In this way, a well constrained dynamical model takes importance as a key step towards the understanding of the Milky Way and therefore the rest of disk-type galaxies.

Aims. To develop a numerical code for modelling the potentials associated to several galactic components. Also to characterize the interaction between test particles and the gravitational potential to obtain dynamical quantities, such as stellar orbits, velocities, energies and angular momentum.

Methods. We use the Runge-Kutta 4 algorithm to solve the motion equations of test particles subject to the forces produced by the stellar bulge, disk and dark matter halo. Also, computational resources were employed in order to perform a detailed analysis.

Results. We analyze three cases in which test particles were introduced to the galactic potential with different initial conditions. As a result of our analysis, we get a set of trajectories, circular velocities, and a good level of confidence in both energy and angular momentum conservation. Finally, a further analysis was made over the orbital behavior based on Poincaré diagrams.

Key words. galactic evolution – stationary potentials – Milky Way

1. Introduction

Since more than four centuries, the forces in the nature have tried to be explained with different physical formulations. One of them is the law of the Universal Gravitation. Isaac Newton (1679) provides this law, he says that the force of mutual attraction acting upon two material points are directly proportional to the product of the masses of such particles and inversely proportional to the square of the distance between them. Galaxies are the systems that we are interested for explaining with this type of laws, in particular, the Milky Way. There is a great importance to understand the structure, dynamics and the evolution of the galactic systems. The proof that the Milky Way is consisting of many faint stars came in 1610 when Galileo Galilei used a telescope to study it. Thomas Wright (1711-1786) speculates that the Milky Way might be a rotating body of a huge number of stars, held together by gravitational forces. Another important author in the study of this galaxy was William Herchel (1785), he makes a first attempt to describe the shape of this galaxy by a carefully counting of stars in different regions of the visible sky. Many authors over the years have studied the Milky Way but it was not until earlies 1930's that the first dynamical description was built by Oort (1932).

Together with the increasing understanding of the dynamical evolution of the Galaxy, more accurate analytical models were arising in order to describe the improved observational studies.

Furthermore, most of the mass in a galaxy lies in the stars, and one of the main goals is to study the behaviour of the gravitational forces of a large clustering of them. Hence, it is necessary to know the morphology and the stability of the stellar orbits in order to develop a theory about the evolution of the galaxies as a whole. A first approach is to study stars as point masses, but this is not practical because for a typical galaxy we have about 10^{11} stars. It is important the study of the gravitational field of the Galaxy because it contains implicit information about stellar orbits (Schmidt 1966), mentioning that if we are dealing with a self-gravitating system, then the gravitational field and the mass distribution are related through Poisson's equation. We must remark that direct information about the distribution of mass mainly consists of the local densities of gas and different kind of stars. Since a large part of the mass distribution in the Galaxy is unobservable, we must study the Galaxy and its components through theoretical models. Some authors have developed theoretical models to explain the interaction of the gravitational field in distinct components of the galaxy (Plummer (1911), Allen & Martos (1986), Allen & Santillan (1991) and Miyamoto & Nagai (1975)). Is in this sense that computational tools became important to predict individual trajectories of each star, and different techniques are needed to be developed. Smooth Particle Hydrodynamics (SPH), N-Body and Magnetohydrodynamical (MHD) codes appeared as powerful implements. Although the first analytical models were nicely understood, the dynamical influence of the Dark Matter (DM) started to play a fundamental role to complete a reasonably general view of the galactic evolution. Navarro, Julio F., Frenk, Carlos S., White (1996), propose a DM Halo model from the "Millenium Simulation"

* e-mail: ecanul@astro.unam.mx

** e-mail: aaroche@astro.unam.mx

*** e-mail: gerardo.urrutia@nucleares.unam.mx

**** e-mail: gmartinez@astro.unam.mx

data which is one of the most DMH used in the current literature.

2. The Milky Way

Since the human being watched carefully the celestial vault, an enigmatic picture was clearly observed passing through the entire night skies, our own Galaxy, and was in the ancient Greece that this structure was named as nowadays we know it: The Milky Way. The Milky Way¹ is a disk barred-armed galaxy with a central bulge approximately spherical and the radial scale of the disk is about 15 kpc (1 pc = 3×10^{18} cm) and its thickness is about 1 kpc. It is estimated that there are around 10^{11} stars, $10^{10} M_{\odot}$ of spread gas and the total (dynamical) mass is calculated around $10^{12} M_{\odot}$ ($M_{\odot} = 2 \times 10^{33}$ grs). Our Galaxy has too a black hole of about $10^6 M_{\odot}$ in the center of the disk, and the bar with $10^{10} M_{\odot}$, contains this while passes through the whole bulge, connecting two prominent spiral arms between them, which are thought to be exponentially distributed around 12 kpc along the disk, rotating with a particular angular velocity of $20 \text{ kms}^{-1} \text{ kpc}^{-1}$ and having between 2-5 % of the mass of the disk. Another constituents of the Galaxy are the dust, galactic magnetic field, charged particles and an additional element, which is responsible for an extra component of the rotation curve, the dark matter halo, which interacts only gravitationally with baryonic matter (stars, gas, dust etc), but its nature remains completely unknown.

3. Theory, simulations and observations

The simplest way to describe a galaxy is by the decomposition in their basic components that affect the gravitational field. These components are well defined by differentiable potential, which is related by a continuous and smooth mass distribution. Then, the galactic dynamics depends on its first derivative, obeying the superposition principle, i.e. the dynamical contribution of each potential to the galactic dynamics, is due to a linear sum of these. The description of a potential due a point-mass particle is well known in the literature, falling as $1/r$. The dynamical description in this case is explained assuming a low-mass particle orbiting around a massive one, typically satisfying the Kepler's laws.

Stellar dynamics (or any deterministic physical system) is described from the solution of Newton's equations (in any canonical variables) [Marion, Classical Dynamics 5 ed.]. These equations go from the most trivial to the most complicated case. We can obtain the expression of the force from a smooth and continuous density distribution [Binney and Tremaine p. 30-31].

For a galactic description, one must think in large scales, then the stars have a behavior, on first approximation, like a test point particles, where the star encounters are negligible. Because of its symmetry and stability, a spherical distribution can be considered as a good approximation; this is the case described by a generalized model known as Miyamoto-Nagai, and the density is obtained using Poisson's equation [Binney and Tremaine p. 42].

A particular case is the Plummer model (Plummer 1911) that states a homogeneous sphere, with soft edge. If in this model $b > r$ then the central density is constant, and when $b \ll r$ is $\propto r^{-5}$ falling at larger radii. To describe the disk, three spatial euclidean axis can be considered, such that the matter distribution vanishes in z values, i.e. we need a mass distribution in the xy plane. The

Kuzmin model describes just this configuration when the stars lie in the galactic disk.

For a dark matter halo (Binney and Tremaine Chapter 2.), a density profile that obeys a power law expression (α exponent) is used. The density profile takes the form $\rho(r) = \rho_0(r_0/r)^{\alpha}$ and a more detailed model, is a combination of two power laws (α and β) given by $\rho = \rho_0/[(r/a)^{\alpha} + (r/a)^{\beta}]$ with a radial scale a . The α parameter is set $\alpha < 3$ to prevent that the mass tends to infinity when the radius tends to zero, and $\beta \geq 3$ to avoid that the mass tends to infinity when the radius is finite. Choosing three special combinations of this exponent values, three different situations can be described. If $\alpha = 1$ and $\beta = 4$ this leads to Hernquist model, with $\alpha = 2$ and $\beta = 4$ leads to Jafee model, and the third, the Navarro, Frenk and White (NFW) model (Navarro, Julio F., Frenk, Carlos S., White 1996) is defined taking $\alpha = 1$ y $\beta = 3$.

Comparisons between theoretical models with observations can range from the simplest with high symmetry models. An example is the Plummer model when his approximation is applicable to fit globular clusters observations (Plummer 1911).

The Plummer model comes closest to representing the observed density profiles of star clusters, currently they are used for example in Kacharov et al. (2014).

The behavior of the density near the center does not match observations of elliptical galaxies, which typically exhibit a diverging central density. Aarseth et al. (1974) have implemented a Monte-Carlo method using the Plummer sphere for construct a N-body simulations, despite the model's lack of realism.

For orbit calculus an example is given in Irrgang et al. (2012). They use the Allen & Santillan model (Allen & Santillan 1991), because of its simple and analytical mathematical treatment that makes it ideally suited for fast and accurate orbit calculations. A big amount of potential models can be found in the literature, able to reproduce just the basic dynamical quantities such as trajectories and rotation curves inherited from the axisymmetry properties. N-body simulations, is motivated from the solution of dynamic of several mass point particles, under their mutual gravitational interaction. This simulations are supported by a self-consistent potentials, nevertheless always present difficulties in resolution. In recent years, the computing power has increased the number N, but the resolution remains a matter to be discussed. An advantage is the natural formation of transitory bars and arms. MHD simulations use hydrodynamic models coupled with electromagnetic fields by continuity equations of both theories. With this construction, the gravitational potential is imposed and the movement integrals are preserved (in a suitable frame-work). Also, one can consider other galactic components as electric and magnetic fields that affect the gas component. The resolution in MHD simulations is greater than N-body simulations. In addition, there is a discussion about the non compliance of the self-consistency. SPH simulations are taken from N-body simulations, but these typically are used for simulations of structure in a cosmological context.

Many models of the Milky Way can be found in the literature, constructed from distinct ideas. Some examples are cited in the following paragraphs.

Bahcall & Soneira (1980) give parameters that describe the disk and the stellar halo, based on star counts. In Bahcall et al. (1982) is taken into account the previous work to model a dark matter halo assuming a central constant density and a falling $r^{-2.7}$ power-law at large radius. Their work shows a flat rotation curve.

Kent et al. (1991) constructed a luminosity model for the bulge, based on the data of $2.4 \mu\text{m}$ map of the galactic plane from the Spacelab Infrared Telescope.

¹ Parameters for MW are taken from Binney & Tremaine 2008

Dehnen & Binney 1998 use observational constraints to construct a disk-bulge-halo galactic mass model. Their work includes the circular velocity curve, the velocity dispersion toward the bulge, the Oort constants, the local velocity dispersion tensor, the total force and surface density in the solar neighborhood.

Xue et al. (2008) derive a galactic rotation curve out to 60 kpc radius. Their rotation curve is based on observations of blue horizontal branch (BHB) stars from the Sloan Digital Sky Survey (SDSS).

Some other mass models of the Milky Way, for instance McMillan (2011) presents a method for fitting parametric mass models of the galaxy. He takes a Bayesian approach which allows the use of photometric and kinematic data, finding a total stellar mass of $6.43 \pm 0.63 \times 10^{10} M_\odot$, virial mass of $1.26 \pm 0.24 \times 10^{12} M_\odot$ and local dark matter density of $0.40 \pm 0.04 \text{ GeV cm}^{-3}$.

4. The method

For the purposes of this paper, we have constructed a galaxy model with only three dynamic components: Stellar bulge, disk and dark matter halo. Each one of them represented by a stationary potential. Also, because of the amount of information that can be obtained, we have decided to restrict our analysis to three interesting cases over the initial conditions, leaving the remaining analysis for a future work.

The three cases mentioned above consist in a particle placed at 8 kpc from the galactic center, with three different initial velocities: total circular velocity $V_{c,T}$, less than $V_{c,T}$, and greater than $V_{c,T}$. As will be seen, these three cases are particularly interesting due to the distinct behavior of the trajectories, energies, and angular momentum over the whole evolving time.

4.1. Galaxy model

We have employed the Plummer model (Plummer 1911) for representing the stellar bulge, and the Kuzmin potential for the disk. Both are a simplification of the Miyamoto-Nagai model (Miyamoto & Nagai 1975), depending on the values of the parameters a and b , which has the form,

$$\phi_{MN} = -\frac{GM_T}{\sqrt{r^2 + (a + \sqrt{z^2 + b^2})^2}}. \quad (1)$$

For simplicity, the analysis has been centered on the x-y plane, setting $z = 0$. Note that in the Miyamoto-Nagai potential, when $a = 0$, it is reduced to the Plummer potential, and similarly, when $b = 0$, it is reduced in a Kuzmin potential for the disk. Thus, the stellar bulge ϕ_b and the disk ϕ_d potentials are,

$$\phi_b = -\frac{GM_b}{\sqrt{r^2 + b^2}} \quad (\text{Plummer}), \quad (2)$$

$$\phi_d = -\frac{GM_d}{\sqrt{r^2 + a^2}} \quad (\text{Kuzmin}). \quad (3)$$

where M_b is the bulge mass, M_d the disk mass, r the radial coordinate from the galactic center, and b and a the Plummer and Kuzmin parameters, respectively. We stress that a and b are related in such a way that varying both parameters, we can reconstruct morphologies from disk-type to spherical galaxies.

Also, we have employed the Navarro-Frenk-White model (cited), which is a well known potential ϕ_{dm} for describing the dark matter halo,

$$\phi_h = -4\pi G\rho_0 a_h^2 \frac{\ln(1 + r/a_h)}{r/a_h} \quad (\text{NFW}), \quad (4)$$

where ρ_0 is defined as 200 times the critical density of the Universe, and a_h is a characteristic radius where the previous condition is fulfilled.

4.2. Equations of motion

From the equations above, one can easily obtain the equations of motion in the x-y plane by differentiating, $F = -\nabla\phi$, each one of the potentials considered. For example, the force by unit mass in the X_i (i.e. x or y) direction experienced by a test particle in the Plummer potential given by equation (2) is,

$$F_{X_i, \text{bulge}} = -\frac{d\phi_b}{dX_i} = -\frac{GM_b X_i}{(x^2 + y^2 + b^2)^{3/2}} = \frac{d^2 X_i}{dt^2}, \quad (5)$$

which is a second-order differential equation that can be converted in two one-order differential equations applying a variable change: $X_1 = X_i$ and $X_2 = X'_i$. Thus,

$$X_1 = X_i \rightarrow X'_1 = X'_i = X_2, \quad (6)$$

$$X_2 = X'_i \rightarrow X'_2 = X''_i = -\frac{GM_b X_i}{(x^2 + y^2 + b^2)^{3/2}}. \quad (7)$$

Note that solving the differential equations for X'_1 and X'_2 will bring the position and the velocity over the X_i axis, respectively.

Due to the similitude in the Kuzmin potential given by equation (3), similar steps can be followed to obtain the motion equations for the disk,

$$F_{X_i, \text{disk}} = -\frac{d\phi_d}{dX_i} = -\frac{GM_d X_i}{(x^2 + y^2 + a^2)^{3/2}} = \frac{d^2 X_i}{dt^2}. \quad (8)$$

Moreover, the force due to dark matter potential in equation (4) is given by,

$$F_{X_i, \text{halo}} = -\frac{d\phi_{dm}}{dX_i} = (4\pi G\rho_0 a_h^2) \left[\frac{X_i}{(x^2 + y^2) \left(1 + \frac{\sqrt{x^2 + y^2}}{a_h}\right)} - \frac{a_h X_i \ln \left[1 + \frac{\sqrt{x^2 + y^2}}{a_h}\right]}{(x^2 + y^2)^{3/2}} \right]. \quad (9)$$

Finally, the total force in the X_i direction due to each galaxy component is just a linear sum of the forces found in equations (5), (8) and (9),

$$F_{T, X_i} = -\frac{d\phi_b}{dX_i} - \frac{d\phi_d}{dX_i} - \frac{d\phi_h}{dX_i}, \quad (10)$$

which can be easily solved applying variable changes as in equations (6) and (7). Note that equation (10) is in fact a set of four coupled one-order differential equations (position and velocity in both x and y direction), which must be solved simultaneously.

4.3. Velocities

An important property of the spherical potentials is that circular velocity can be derived from the current potential where the particle resides,

$$V_c = \sqrt{r \left| \frac{d\phi}{dr} \right|}. \quad (11)$$

Thus, for each galaxy component, the independent circular velocities of the bulge, disk and halo are respectively,

$$V_{c,b} = \sqrt{\frac{GM_b r^2}{(r^2 + b^2)^{3/2}}}, \quad (12)$$

$$V_{c,d} = \sqrt{\frac{GM_d r^2}{(r^2 + a^2)^{3/2}}}, \quad (13)$$

$$V_{c,h} = \sqrt{4\pi G \rho_0 a_h^3 \left[\frac{1}{a_h(1 + r/a_h)} - \frac{\ln(1 + r/a_h)}{r} \right]}. \quad (14)$$

By the additivity property of the stationary potentials,

$$\phi_T = \phi_b + \phi_d + \phi_h, \quad (15)$$

the total circular velocity is computed from the entire galaxy potential ϕ_T as,

$$\begin{aligned} V_{c,T} &= \sqrt{r \left| \frac{d\phi_T}{dr} \right|} = \sqrt{r \left| \frac{d\phi_b}{dr} \right| + r \left| \frac{d\phi_d}{dr} \right| + r \left| \frac{d\phi_h}{dr} \right|} \\ &= \sqrt{V_{c,b}^2 + V_{c,d}^2 + V_{c,h}^2}. \end{aligned} \quad (16)$$

Also consider the minimum velocity required for a particle to overcome the galactic potential well, i.e., the scape velocity,

$$V_e = \sqrt{2|\phi_t|} = \sqrt{2|\phi_b| + 2|\phi_d| + 2|\phi_h|}. \quad (17)$$

4.4. The code

We developed a numerical code in Python 2.7.5 that solves the equations of motion for a test particle subject to the interaction of stationary potentials, based on the Runge-Kutta 4 algorithm with fixed step. We decide do not implement the Runge-Kutta-Fehlberg algorithm with variable step due to the complexity for solving coupled differential equations. However, we test our code varying the step lenght, and we do not report any significant difference in the computing time and results. Even the uncertainties in all involved variables agree with those accepted in the literature.

The code receives six main input parameters: M_b , M_d , ρ_0 , a , b , a_h . All those are necessary to compute the galactic potentials. Also, initial conditions of position and velocity for the test particle must be specified. Once the evolution time has been established, the code calculates the orbit in the x-y plane, the rotation curve, and both energy and angular momentum for the test particle. In addition, we implemented a subroutine which creates a grid in radius and construct a Poincaré diagram for further analysis.

Parameter	Value	G. units
Bulge mass (M_b)	$3 \times 10^{10} M_\odot$	$1293 M_u$
Disk mass (M_d)*	$5 \times 10^{10} M_\odot$	$2155 M_u$
Plumer parameter (b)	1.5 kpc	1.5 kpc
Kuzmin parameter (a)	$b/0.2$	7.6 kpc
NFW char. radius (a_h)*	r_{200}/c	22.5 kpc
NFW char. density (ρ_0)*	$0.006 M_\odot \text{ pc}^{-3}$	$.258 M_u \text{ kpc}^{-3}$

Table 1. Input parameters. Assumed values for the current analysis. For clarity, values have been also written in the galactic unit system. *Data from Xue et al. (2008). Remaining values were proposed from our rotation curve analysis.

5. Analysis and Results

5.1. Model assumptions

For a complete analysis, we adopted a set of realistic parameters (see Table 1) used in several galaxy evolution models. However, we proposed some of those input parameters in order to fit a semi-flat rotation curve, stressing that our analysis is not substantially affected by the chosen parameters.

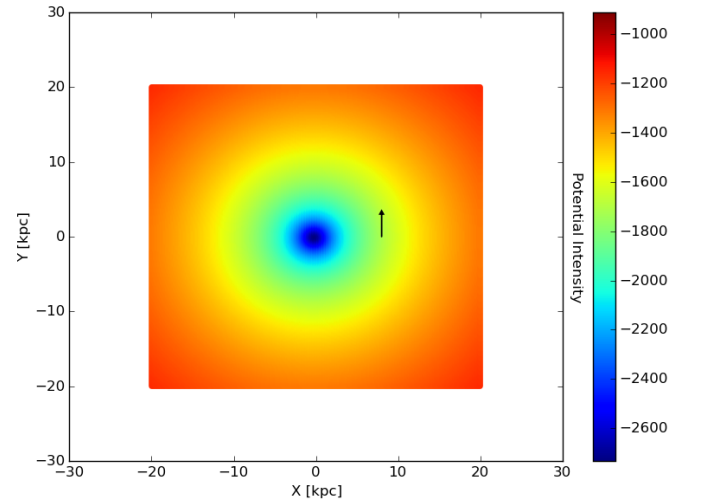


Fig. 1. Color map of the total galactic potential composed of three galactic structures. The black arrow represents the initial radius and direction where the test particles were launched (see text for reference).

We converted the input parameters into *galactic units*, which help to avoid numerical under/over-flow troubles. The galactic units system is as follows:

$[M] = 2.32 \times 10^7 M_\odot$	Unitary mass M_u
$[D] = 1 \text{ kpc}$	Distance
$[V] = 10 \text{ km/s}$	Velocity
$[T] = 10^8 \text{ years}$	Time
$[G] = 1 D^3 / M_u T^2$	Gravitational constant.

Values converted to this system are showed as comparison in third column of Table 1.

To visualize the total galactic potential of our study, we built a color map over the x-y plane (see Figure 1) which shows the potential intensity over the first 20 kpc from the center. Note

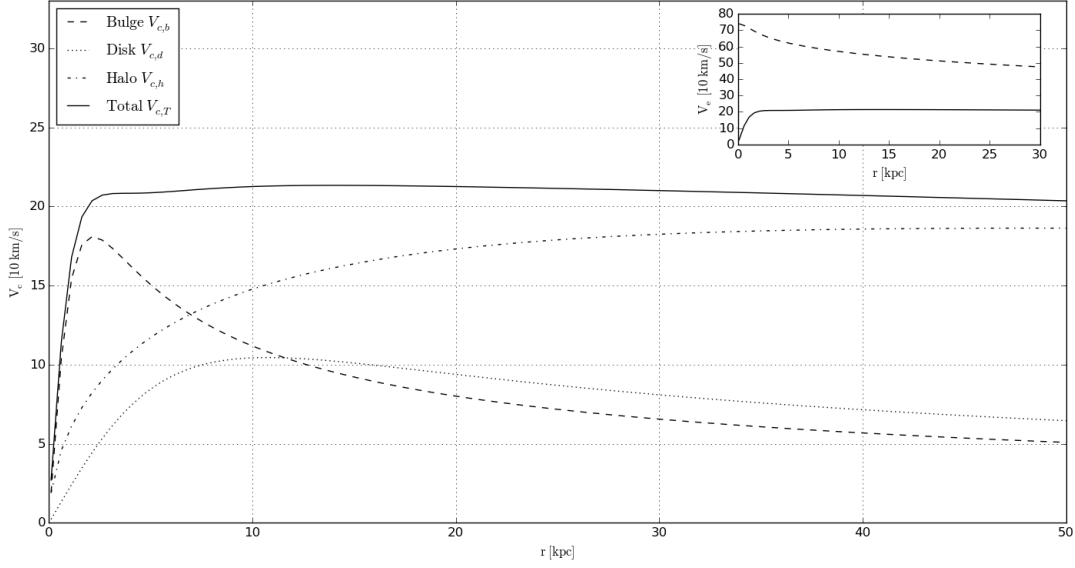


Fig. 2. Rotation curve of the constructed galaxy. Circular velocities (in units of 10 km/s) of individual components are shown in different line styles. Solid line is the total circular velocity of the galaxy. For comparison, subplot shows the total circular velocity (solid line) and escape velocity (dashed line).

that three remarkable regions can be detected where each galactic structure dominates: central stellar bulge (blue region), disk (green-yellow region) and halo (red region).

Individual rotation curves were calculated for each galactic component. In Figure 2 we overplot all the circular velocities for bulge, disk and halo, as well as the total rotation curve from equation (16). It is well known that most spiral galaxies exhibit a semi-flat rotation curve, discrepant from the classical newtonian expectation. We took advantage of this fact to vary three free parameters (as specified in Table 1) in order to reproduce the circular velocity of 220 km/s at 8 kpc .

As mentioned previously, we focus our study in three different initial condition cases. For all of them, the test particle was launched at 8 kpc over the x axis from the galactic center in the positive y axis direction (illustrated by the black arrow in Figure 1). Also, the evolution time has been set to 1×10^{10} years.

We define, *Case A*: particle with initial velocity set exactly to the total circular velocity $V_{c,T} = 211.301 \text{ km/s}$ at 8 kpc . *Case B*: particle with a initial velocity less than $V_{c,T}$. *Case C*: particle with a initial velocity greater than $V_{c,T}$. The adopted initial velocities are: $V_{c,T} = 211.301 \text{ km/s}$, $V_{c,T} - 120 \text{ km/s}$, and $V_{c,T} + 120 \text{ km/s}$ for the *A*, *B* and *C* cases respectively.

5.2. Trajectories

We evolve the system during 1×10^{10} years, and every 1×10^{-5} years the particle reports its current position in the x - y plane by a transparent point. In Figure 3 we show the peculiar trajectories found over the whole computed time (see Appendix A for a complementary picture of the orbits). Subplots are labeled with the considered case and assumed initial velocity. As expected, *Case A* reproduce a circular trajectory due to the precise circular velocity calculated from the total potential. Without energy losses, circular orbit will be stable forever. However, we found that varying slightly the initial speed (even a thousandth in precision), the final orbit configuration moves toward cases *B* or

C. Contrary, *Case B* and *Case C* manifest an astonishing donut-shaped orbit, which evolve between two noticeable radii. The inner and outer radii can be calculated from the minimum and maximum radial energy.

A characteristic behavior can be observed from the two last cases: in *Case B* the orbit evolve outside-in, i.e., the test particle moves inside its 8 kpc initial radius, while in *Case C* the particle moves inside-out and its initial radius becomes a lower limit over all possible trajectories. Another interesting behavior is that particles with velocities less than $V_{c,T}$ tends to fill the whole allowed space. In contrast, if the particle is initially provided with a velocity greater than $V_{c,T}$, the orbits will not fill the entire space, although both particles have the same evolution time. It is a geometric problem, since particles even with high speed have to travel over more space in the same time.

5.3. Energy and Angular momentum conservation

We test our code in order to find possible energy and angular momentum leaks. Given that the code provides of speed components (V_x and V_y) at each time step, we are able to allocate kinetic energy per mass unit to the particle since,

$$E_C = 0.5 \sqrt{V_x^2 + V_y^2}. \quad (18)$$

In addition, potential energy is computed from equations (2), (3), and (4), which just need the location of the particle ($r = \sqrt{x^2 + y^2}$), also provided by the code. Finally, the total energy is calculated from the sum of both the kinetic and potential energies.

In other hand, the z component of angular momentum per mass unit is estimated as,

$$\bar{L} = \bar{r} \times \bar{p} = \hat{k}(xV_y - yV_x) = L_z \quad (19)$$

where the last equality arises from the fact that the particle is moving on the plane.

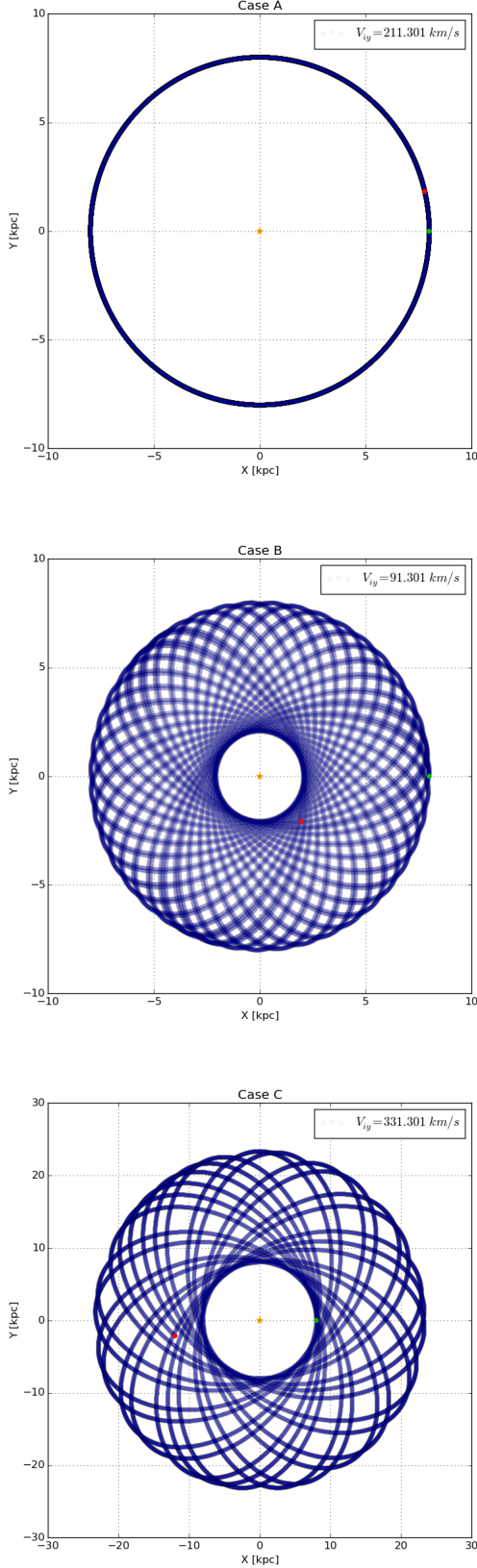


Fig. 3. Trajectories of distinct test particles subject to the same galactic potential. From top to bottom, cases A, B, and C are illustrated. Green point placed at 8 kpc over the x axis shows the initial position where the particle is launched. Red point indicates the final location after 1×10^{10} years of evolution.

In Figure 4 we show the first 30×10^8 years of evolution and the curves of energy and angular momentum for the three cases. To determine if both quantities were suitably conserved, we made a sanity check by calculating the total initial energy and angular momentum and compared with the values at the end of the evolution time. Relative error is a good tracer of the conservation laws, so we use the standard definition,

$$\Delta E = \frac{E_{init} - E_{final}}{E_{init}}, \quad \Delta L = \frac{L_{init} - L_{final}}{L_{init}}. \quad (20)$$

The results of the conservation analysis (see Figure 4) suggest that our current study falls inside the error limits accepted by the community, since we have obtained errors around $\log(\Delta E) \approx -10/-13$, and $\log(\Delta L) \approx -10/-14$. We recall that those numerical losses have been computed over 1×10^{10} years of evolution. Hence, our results can be taken with a good degree of reliability.

Particularly, the energy evolution shows a distinctive behavior for the three cases. In the circular orbit case, all energies remain constant as expected from the property of axisymmetric potentials. Also, the kinetic energy remains invariant due to the imposed circular velocity. In the two last cases, the main characteristic resides on the oscillations of energy, which are associated with the exchange between kinetic and potential energy while the particle moves away or approaches to the center. A detailed inspection of *Case C* reveals that kinetic energy has its minimum when the potential energies reach their maxima. Note also that the period of such energy oscillations are in concordance with the orbital periods showed in Figure 3. In other words, the particle in the *Case B* performs more orbits around the galactic center than the particle in *Case C*, and the respective orbital periods can be known from the oscillation in the energy evolution.

5.4. Poincaré maps

In this subsection we will give a further analysis in order to characterize the possible orbits inside the potential in study. We use the Poincaré diagram, a powerful tool to visualize the behavior of the orbits over a selected axis. We constructed a grid over the x axis, putting 100 particles equidistantly in a range of 50 kpc. Each particle were launched with the same initial velocity in the positive y direction. Any time a particle cross the x axis (positive or negative) the program ask for both its instantaneous V_x velocity and x position. We consider two cases of special interest: when the initial velocity $V_y = 140$ km/s analogous to the *Case B*, and when V_y is equal to maximum reached velocity in the rotation curve ($V_{c,max} = 213.3$ km/s), considered as *Case C* since the total circular velocity is $V_{c,T} = 211.301$ km/s.

We plotted the instantaneous x component of velocity and position of the whole particles ensemble (see Figure 5). Colors indicate the initial radius where each particle started its trajectory. Clearly, both figures disagree between themselves. In the *Case B* the orbits span a wide velocity range compared with *Case C*. Also the general shape of the Poincaré map in both cases suggest a strong dependency with the assumed velocity. We investigate for a possible physical meaning by exploring the fundamental equations from where the Poincaré map were constructed. Consider the velocity components given by equations (12), (13) and (14). We inverted equation (16) to know $r = R_C$, the circular radius, as a function of $V_{c,T}$,

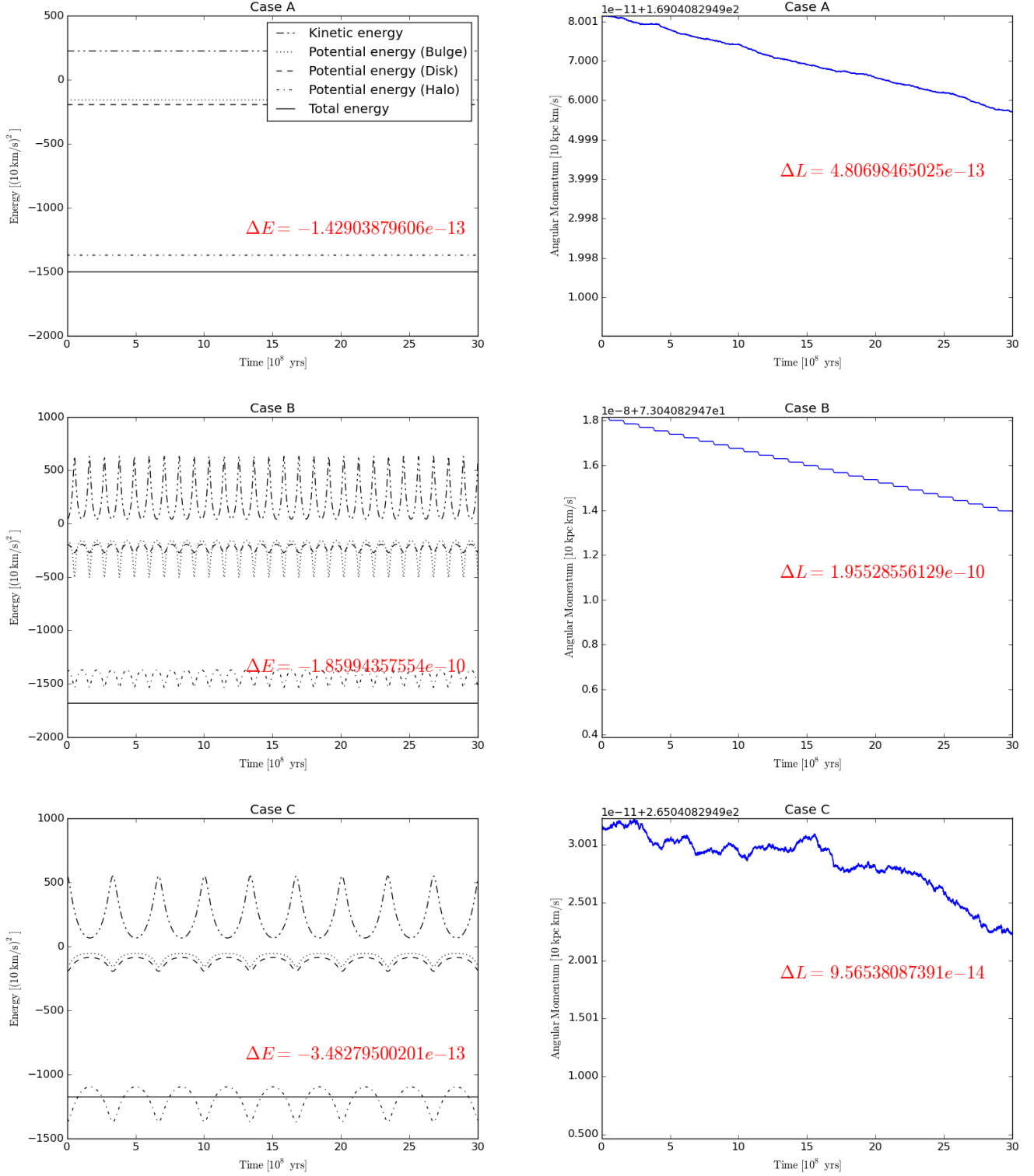


Fig. 4. Energy and angular momentum variations over $\sim 1/3$ of the full evolution time. Figures in left-hand side indicates the variation of energy, while in the right-hand side the angular momentum is showed. Distinct line styles are associated with the energy experienced by the particle due to the three galactic components. From top to bottom, each row represent the A, B, and C cases respectively. Relative errors over the total energy (ΔE) and angular momentum (ΔL) are included in their respective panels.

$$R_C = \sqrt{\frac{V_{c,T}^2 - 4\pi G\rho_0 a_h^3 (f_1)}{Gf_2}}, \quad (21)$$

$$\text{where } f_1 = \frac{1}{a_h(1 + R_C/a_h)} - \frac{\ln(1 + R_C/a_h)}{R_C}, \quad (22)$$

$$\text{and } f_2 = M_b/(R_C^2 + b^2)^{3/2} + M_d/(R_C^2 + a^2)^{3/2}. \quad (23)$$

Note however that those are a set of transcendental equation which must be solved numerically. We employed the fixed point algorithm to approximate R_C . A initial value were supposed and the iteration finished when an accuracy of 10^{-5} was reached. In Figure 5 we indicate the found radius by a vertical dashed line

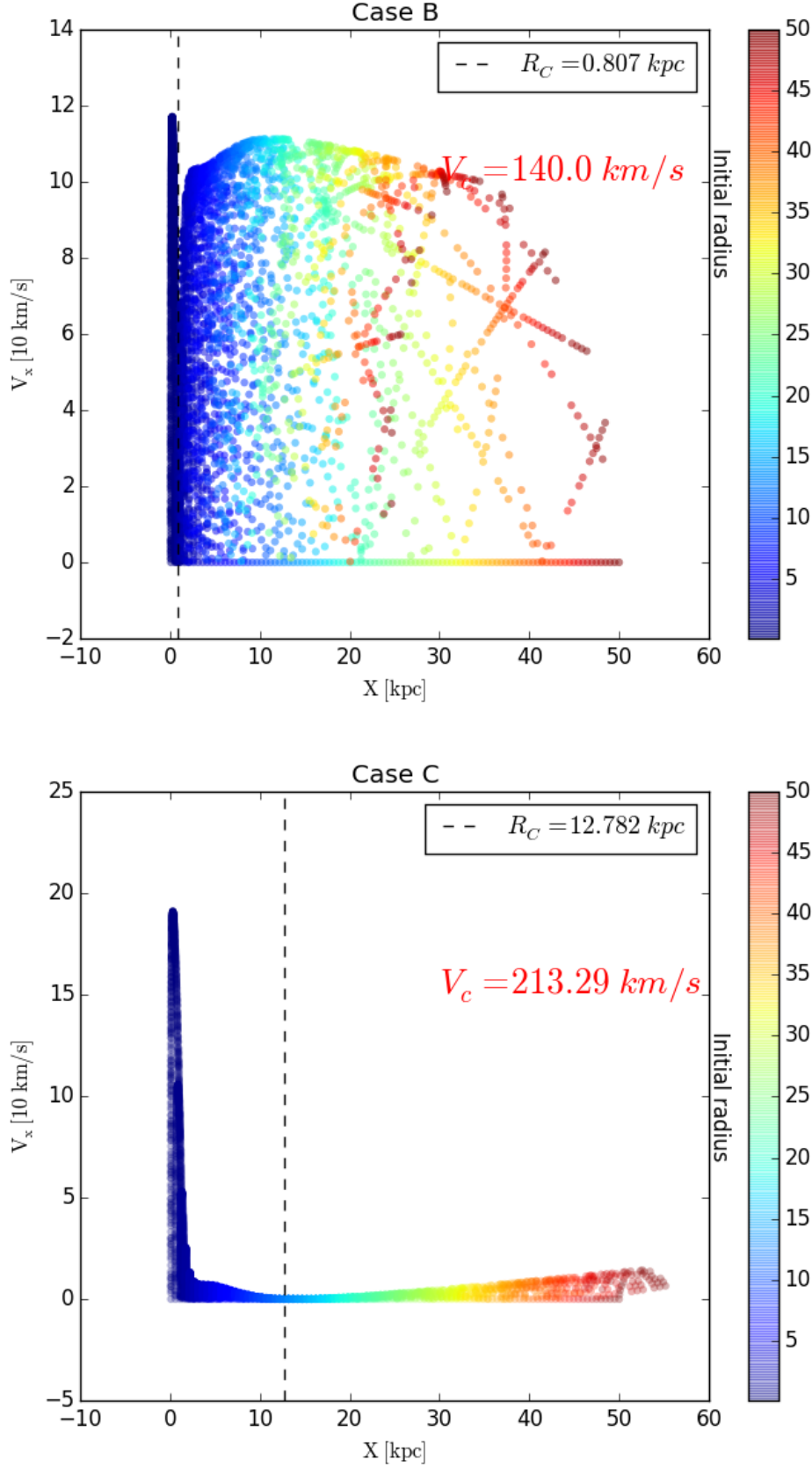


Fig. 5. Poincaré maps of a two set of particles. Top figure display the orbital configuration of particles launched with $V_c = 140 \text{ km/s}$ initial speed. Bottom figure consider the orbits of particles with the maximum velocity $V_c = 213.29 \text{ km/s}$ reached in the rotation curve. Dashed lines are placed at the circular radius R_C where the computed velocities correspond to the circular velocities.

computed from equation (21) with the respective $V_{c,T}$ labeled in both figures.

We repeated the previous technique for several distinct initial velocities and we detected a common dependence. In all Poincaré diagrams the circular radius R_C from equation (21) falls inside the gap of V_x values. See for example in *Case B*, a small notch is formed near the galactic center. Precisely there, the circular radius R_C is located. A detailed analysis in *Case C*, reveals that R_C also falls in the minimum range of V_x . A suitable explanation can be derived considering that R_C is placed where the neighboring orbits tends to be more circular. In this sense, the closest orbits to R_C pass almost normal through the x axis, minimizing the contribution of the velocity in the x direction. The remarkable difference between the width of the allowed velocity V_x in both cases, is a natural consequence of the obliquity with which the orbits cross the x axis, as can be seen from Figure 3.

6. Conclusions

In this work, we have developed a numerical code that solves motion equations of test particles subject to the forces produced by three galactic components: stellar bulge, disk and dark matter halo. Several dynamic quantities were obtained to characterize the interaction between particles and the total galactic potential, such as energy, angular momentum and trajectories. We summarize some important issues:

1. Using accepted values for the potential parameters, a good fit to the rotation curve and its flattened feature was obtained by matching the well-known circular velocity in the solar neighbourhood of $V_{c,\odot} \approx 220 \text{ km/s}$.
2. As expected, if the initial velocity is smaller or larger than $V_{c,T}$, the final trajectories form rosette-type patterns which evolve outside-in or inside-out respectively.
3. We test our code to assess possible energy and angular momentum losses, finding a good agreement with the relative errors reported in the literature since our analysis yields $\log(\Delta E) \approx -10/-13$, and $\log(\Delta L) \approx -10/-14$.
4. Poincaré maps reveal concordance in the conservation of the previous studied quantities. Also the orbit stability is inferred from the well constrained shape in the velocity-position space. Moreover we do not report chaos evidence.

Acknowledgements. We thank the Dr. E. Moreno, Dr. B. Pichardo and Dr. L. Medina for their teachings about galaxy dynamics. Part of this work was supported by the scholarship provided by CONACYT.

A color version of this paper can be obtained at <https://dl.dropboxusercontent.com/u/61324606/aa.pdf>

References

- Aarseth, S. J., Henon, M., Wielen, R., & Landau, L. 1974, *Astronomy and Astrophysics*, 37, 183
- Allen, C. & Martos, M. A. 1986, *Rev. Mexicana Astron. Astrofis.*, 13, 137
- Allen, C. & Santillan, A. 1991, *Rev. Mexicana Astron. Astrofis.*, 22, 255
- Irrgang, A., Wilcox, B., Tucker, E., & Schiefelbein, L. 2012, 5439
- Kacharov, N., Bianchini, P., Koch, A., et al. 2014, *Astronomy & Astrophysics*, 567, A69
- Kent, S. M., Dame, T. M., & Fazio, G. 1991, *ApJ*, 378, 131
- Kim, W. & Ostriker, E. C. 2006, *The Astrophysical Journal*, 646, 213
- McMillan, P. J. 2011, *Monthly Notices of the Royal Astronomical Society*, 414, 2446
- Miyamoto, M. & Nagai, R. 1975, *Astronomical Society of Japan*, 27, 533
- Navarro, Julio F., Frenk, Carlos S., White, S. D. M. 1996, *Astrophysical Journal*, 378, 496
- Oort, J. H. 1932, *Bull. Astron. Inst. Netherlands*, 6, 249

- Plummer, H. C. 1911, *Monthly Notices of the Royal Astronomical Society*, 71, 460
- Roca-F?brega, S., Valenzuela, O., Figueras, F., et al. 2013, *Monthly Notices of the Royal Astronomical Society*, 432, 2878
- Schmidt, M. 1966, *IAU Symposium*, 25, 61
- Xue, X. X., Rix, H. W., Zhao, G., et al. 2008, *The Astrophysical Journal*, 684, 1143

Appendix A

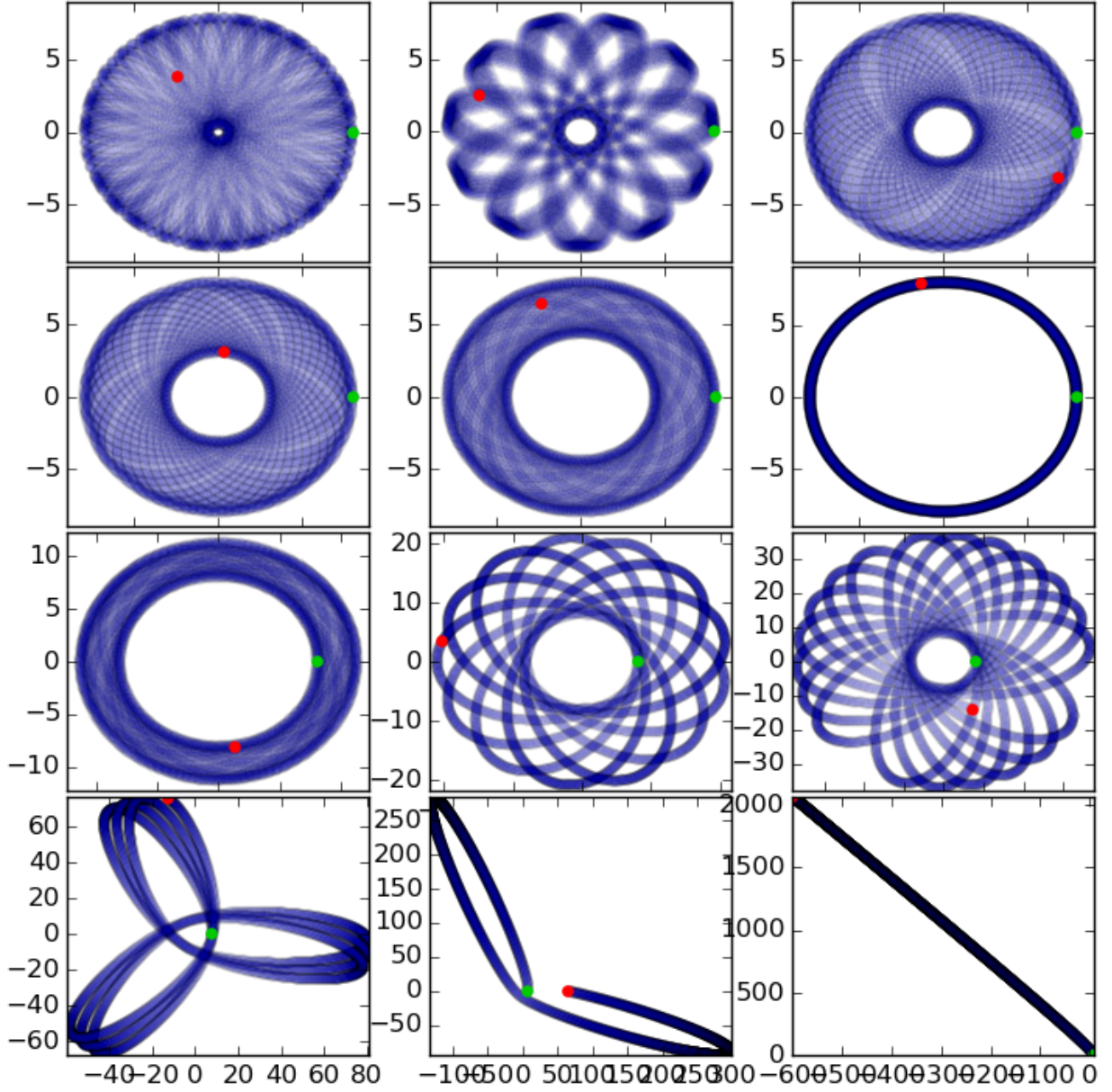


Fig. 6. Some trajectories computed in our current analysis. Both axis are showed in kpc. From left to right and top to bottom, the initial V_y velocities are: 30, 60, 90, 120, 150, 210, 250, 320, 380, 450, 530, 600 km/s.

Different V_y initial values

For a clear visual inspection, we plotted several orbital morphologies varying the initial V_y velocity, but as before, placing the particle at 8 kpc from the center over the x axis. The evolution time is also 1×10^{10} years. Some trajectories can be observed in Figure 6. We observe the smooth transition of the orbits spanning almost the entire space, towards a circular orbit configuration (showed in the first 6 subplots from left to right and top to

bottom). After that, the orbits increase their radius until the velocity escape is reached (given by equation (17)) as can be seen in the bottom right corner, where the velocity exceeds 500 km/s.